Observing system simulation experiments in geomagnetic data assimilation

Don Liu,[1] Andrew Tangborn,[1] and Weijia Kuang[2]

Received 11 August 2006; revised 14 May 2007; accepted 30 May 2007; published 29 August 2007.

[1] Observing System Simulation Experiments (OSSEs) have been carried out for a geomagnetic data assimilation system. The purpose of these experiments is to demonstrate how new algorithms for assimilating geomagnetic observations into a geodynamo model can be evaluated. A "nature" run is carried out to establish a "true" evolution of the Earth's core state, from which synthetic surface geomagnetic field observations are created. These observations are then assimilated into the geodynamo model using an optimal interpolation (OI) scheme. Model error is simulated by using a different Rayleigh number in the nature and model runs. Because the true core state evolution is known completely, the assimilation results can be evaluated in terms of any state variable and at any point in the computational domain. In this work we focus on the poloidal (observed) and toroidal (unobserved) components of the magnetic field throughout the outer core. Experiments are carried out using observations of different degrees and varying forecast error correlation length scales. We also investigate the impact of model error on the assimilation and on the accuracy of geomagnetic forecasts. Assimilation runs lasting about 90% of the magnetic free decay time show a positive impact on both components of magnetic field deep within the outer core. Forecasts of the surface magnetic field show much lower error growth, indicating that the initial condition used for the forecasts has been substantially improved through assimilation.

Citation: Liu, D., A. Tangborn, and W. Kuang (2007), Observing system simulation experiments in geomagnetic data assimilation, *J. Geophys. Res.*, *112*, B08103, doi:10.1029/2006JB004691.

1. Introduction

[2] The Earth has possessed an internal magnetic field (geomagnetic field) through much of its history. This field is believed to be generated and maintained by convection in the iron-rich fluid outer core (geodynamo). Dynamo theory first appeared nearly 90 years ago [*Larmor*, 1919], but nonlinear, self-consistent numerical models have been successful only in the past decade [*Glatzmaier and Roberts*, 1995; *Kageyama and Sato*, 1997; *Kuang and Bloxham*, 1997; *Dormy et al.*, 2000]. Current numerical dynamo models generate magnetic fields that are qualitatively similar to the geomagnetic field observed at the surface of the Earth, e.g., a dominantly axial dipole poloidal magnetic field. However, the similarity between the model output and the observation ends right at the dipole dominance.

[3] This raises several critical questions: Why the model output differs significantly from observation? In other words, in addition to the differences between the parameter values used in numerical models and those appropriate for the outer core, could other physical approximations play major roles? Can we learn more about the true physical state in the outer core via numerical modeling? Can and how we use surface geomagnetic observation to constrain numerical models? One approach to address these questions is data assimilation, which can provide important knowledge on the accuracy of the numerical estimations of the true state of the core, and on possible improvement of such estimations with geomagnetic observations.

[4] Data assimilation has been widely used in meteorology and oceanography over the past half century. Numerical weather prediction was in a significantly worse state 50 years ago, when numerical models were extremely crude in terms of both resolution and the realism of the parameterized physics. Even so, early data assimilation methods were being developed in order to combine model outputs with the relatively few observations that were available at the time (see *Talagrand* [1997] for a historical summary). Since then, enormous improvements have been made in modeling, observations, and assimilation methodology; and the development of each of these fields was enhanced by interactions with the others. For example, many new satellite missions are designed specifically to be used in assimilation systems in order to improve numerical weather prediction. Thus it appears that data assimilation is an appropriate and needed component that can help to improve both geodynamo modeling and geomagnetic observations. Recent investigations into the use of data assimilation in simplified MHD systems [*Fournier et al.*, 2007; *Sun et al.*,

[1]Joint Center For Earth Systems Technology, University of Maryland, Baltimore County, Baltimore, Maryland, USA.
[2]Planetary Geodynamics Laboratory, NASA Goddard Space Flight Center, Greenbelt, Maryland, USA.

Copyright 2007 by the American Geophysical Union.
0148-0227/07/2006JB004691$09.00

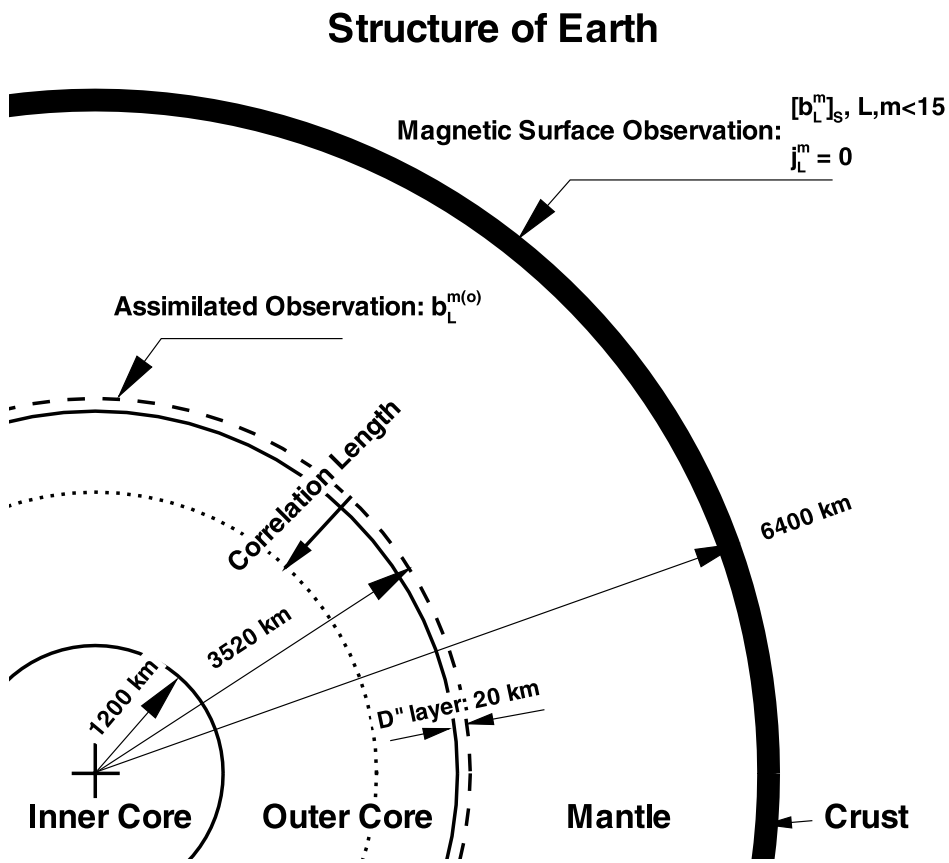

Figure 1. Sketch of the Earth's interior.

2007] have shown that magnetic field observations can be used to improve velocity field estimates. The purpose of the present work is to demonstrate how geomagnetic data assimilation methods can be developed and tested, given the current state of geodynamo modeling and the historical record for geomagnetic observations.

[5] Data assimilation is a mathematical method for combining model prediction (or forecast) with physical observations with the explicit goal of obtaining the best possible estimate of the state of a system. If this combination is done in a dynamically consistent way (e.g., without violating conservation laws or creating nonphysical steep gradients), this new estimate (called the analysis) can be used as an initial condition for a model run that will forecast future states of the system. Data Assimilation systems generally use Bayesian estimation theory, and therefore require error estimates of both the forecast and observations. These error estimates are used in a cost function which is minimized so as to obtain an analysis state with the minimum error variance.

[6] In typical assimilation systems not all of the state variables are observed, and measurements are often made in only a small part of the domain. For example, in atmospheric data assimilation, wind velocity is typically made near the surface, but not high in the Stratosphere. Ocean data assimilation systems have even more sparse observing networks, being mostly at the surface. It is very common that most of the state of the system is unobserved, and it is difficult to know whether the assimilation of a particular set of observations has had a positive impact (by reducing errors) on the state estimate everywhere. Typical validation experiments will use a second (unassimilated) data set to characterize the assimilation success. However, this approach is only useful if the observations are both global and have relatively small (unbiased) errors.

[7] Geomagnetic data assimilation faces far more challenges, largely due to the severe limitations on observable variables (poloidal component of magnetic field only), observation locations (Earth's surface), and the relatively low spatial and temporal resolution of the observed variables. For example, as shown in Figure 1, the fluid outer core and the surface of the Earth are separated by a thick mantle, which is nearly perfectly electrically insulating. The electrical conductivity of the mantle is on average at least 4 orders of magnitude lower than that of the core [*Shankland et al.*, 1981]. Thus only large-spatial scale, low-frequency signals of the poloidal magnetic field $\boldsymbol{B}_P$ can be clearly detected at the surface. In addition, near the surface, crustal magnetism (via induction and magnetization of the crust) contaminates the signals, further limiting the geomagnetic observations.

[8] Through much of the mantle and at the Earth's surface, $\boldsymbol{B}_P$ is a potential field, and thus described by a scalar. If the potential scalar is expressed as a spherical harmonic expansion series, the attenuation of the mantle and the contamination of the crust magnetism limit the observations to the spectral coefficients up to degree L_{obs}, i.e., only the coefficients with the degree $l \leq L_{\mathrm{obs}}$ are observables. With the most advanced, near Earth satellite observation, $L_{\mathrm{obs}} \approx 14$, [see, e.g., *Macmillan and Quinn*, 2000].

Going back in time, the resolution is even poorer, e.g. $L_{\mathrm{obs}} = 5$ for archeo/paleomagnetic data. The potential scalar can be continued downward to the top of the D″ layer, or to the core-mantle boundary (CMB) (assuming no electrically conducting layer at the bottom of the mantle). Assessing the success of a geomagnetic data assimilation system is therefore rather challenging, and is in need of an approach that can identify which variables in the state estimate have been improved and whether this new estimate would make a better initial condition for future forecasts of the magnetic field.

[9] One solution to this problem is through the use of synthetic observations, which are created by carrying out a single model run which is defined as the "truth". Observations are then simulated by adding errors to state variables at the locations and times where real observations would be expected. In some cases the observations are not state variables (e.g., rainfall, wind speed), so that an observation model is needed to create these artificial measurements. These synthetic observations are then assimilated into a second model run that differs from the "truth" in the initial state and/or some difference in the model itself. If the only difference is the initial state, then the model is "perfect" and the difference between the truth and forecast should decrease to the size of the observation errors after a sufficient number of assimilation cycles. Model error can be simulated in a number of ways, including the use of a different model, decreasing numerical resolution or altering some parameter in the model. With model error included in the assimilation, errors will tend to grow between assimilation times.

[10] The most common application of synthetic observations is to carry out Observing System Simulation Experiments (OSSEs) which are used to assess the value of a proposed new observing network or test a new assimilation algorithm. Because the "true" values for the entire state of the system are known at every time step, a very detailed analysis can be made on the impact of the assimilation system. Thus not only can the decrease in errors for the observed variables be assessed, but also those of nonobserved variables. In addition, OSSEs allow for the calculation of an error growth rate for forecasts, which is an important criterion for assessing the success of an assimilation system. If the analysis state is drawn closer to the true state in a dynamically consistent manner, then one could expect that a forecast run which uses this analysis as an initial condition to have slower error growth rate. Finally, OSSEs have been instrumental in validation of new assimilation algorithms. Most notable are the ensemble Kalman filter systems [*Evensen*, 1994; *Houtekamer and Mitchell*, 1998] which evolve forecast error covariances using an ensemble of model runs that start from perturbed initial states. A complete description of OSSEs is given by *Atlas* [1997].

[11] Data assimilation algorithms can generally be divided into two main categories, sequential and variational. In sequential methods, a numerical model is run until observations become available (even though the measurements are made at different times), and these are then assimilated with the forecast to create the analysis to be used as the new initial state for the next forecast. Variational methods, in contrast, adjust the model solution over an assimilation window so as to best fit the available observations during this time period. There are pros and cons for each approach, with the former having the advantage of ease of implementation and the latter can potentially help to correct initial state using observations from a later time [*Talagrand*, 1997]. In this paper, we describe a sequential geomagnetic data assimilation system with two different Rayleigh numbers R_{th}: synthetic observations are extracted from a single "true" run with the Rayleigh number $R_{\mathrm{th}}^{(1)}$. The forecast run into which the observations are assimilated is made with the Rayleigh number $R_{\mathrm{th}}^{(2)}$. All other parameter values in these two runs are kept the same. The purpose of the experiment is to understand how corrections to the measured (poloidal) component of the magnetic field will effect other components of the state of the core. We have chosen the model and true Rayleigh numbers to be very close so that the model error is small but nonzero. This allows us to assess the success of the assimilation through subtle improvements to the forecast error growth rate. The experiment is carried out for a large number of assimilation cycles (or analysis steps) and for a significant fraction of the magnetic decay time unit. In section 2 we describe the numerical model and assimilation algorithm, and the experiments are outlined in section 3. Section 4 presents the results of the OSSEs, and the discussion is given in section 5.

2. Mathematical Formulation

[12] The mathematical formulation for the OSSEs includes the numerical geodynamo model and the optimal interpolation algorithm for data assimilation.

2.1. Geodynamo Model

[13] The numerical dynamo model used in this study is the MoSST (Modular Scalable Self-consistent Three-dimensional) core dynamics model developed at Harvard and GSFC. Here we only provide a brief summary of the model. Details are given by *Kuang and Bloxham* [1999] and *Kuang and Chao* [2003].

[14] The geometry of the numerical model is sketched in Figure 1. The fluid outer core is defined as the region between the radius r_{icb} of the inner core boundary (ICB), and the radius r_{cmb} of the core-mantle boundary (CMB):

$$r_{\mathrm{cmb}} \geq r \geq r_{\mathrm{icb}}.$$

It is electrically conducting, with a magnetic diffusivity η_o. The inner core $r \leq r_{\mathrm{icb}}$ is an electrically conducting solid sphere, with a magnetic diffusivity $\eta_i = \eta_o$. The D″ layer $r_{\mathrm{cmb}} \leq r \leq r_{\mathrm{dp}}$ (where r_{dp} is the mean radius of the top of the D″ layer) is also electrically conducting, but with a much larger magnetic diffusivity, e.g., $\eta_d = 20\ \eta_o$. We choose the D″ layer thickness to be 20 km so that the total conductance of the layer (multiplication of electrical conductivity by the layer thickness) is 3 orders of magnitude smaller than that of the core. Other choices of the D″ layer is possible. In general, the lower the η_d (i.e., the higher the electrical conductivity), the thinner the layer. The whole system rotates with a mean angular velocity

$$\mathbf{\Omega} = \Omega \mathbf{1_z},$$

where $\mathbf{1}_z$ is the unit vector along the z axis (the mean rotation axis).

[15] In the reference frame corotating with the Earth, convection in the outer core can be described by the momentum equation, the induction equation and the energy equation, which, after appropriate scaling [*Kuang and Bloxham*, 1999], have the following nondimensional forms:

$$R_o\left(\frac{\partial}{\partial t}+\boldsymbol{v}\cdot\boldsymbol{\nabla}\right)\boldsymbol{v}+\mathbf{1}_z\times v=-\boldsymbol{\nabla}p+\boldsymbol{J}\times\boldsymbol{B}+R_{\mathrm{th}}\Theta\mathbf{r}+E\boldsymbol{\nabla}^2\boldsymbol{v}, \tag{1}$$

$$\frac{\partial\boldsymbol{B}}{\partial t}=\boldsymbol{\nabla}\times(\boldsymbol{v}\times\boldsymbol{B})+\nabla^2\boldsymbol{B}, \tag{2}$$

$$\frac{\partial\Theta}{\partial t}=-(\boldsymbol{v}\cdot\boldsymbol{\nabla})\Theta_0-(\boldsymbol{v}\cdot\boldsymbol{\nabla})\Theta+q_\kappa\boldsymbol{\nabla}^2\Theta, \tag{3}$$

where $\boldsymbol{v}$ is the velocity field, $\boldsymbol{J}$ ($\equiv\boldsymbol{\nabla}\times\boldsymbol{B}$) is the current density, Θ is the temperature perturbation (density anomaly), Θ_0 describes the prevailing conducting state in the outer core, $\mathbf{r}$ is the position vector. There are also several parameters in (1)–(3) that result from the nondimensionalization: the Rayleigh number R_{th} that measures the buoyancy force, the magnetic Rossby number R_o that describes the relative importance of the fluid inertia to the Coriolis effect, the Ekman number E that describes the relative importance of the fluid viscosity relative to the Coriolis effect, and the modified Prandtl number q_κ is the ratio of the thermal diffusivity to the magnetic diffusivity:

$$R_{\mathrm{th}}\equiv\frac{\alpha_T g_0 h_T r_{\mathrm{cmb}}^2}{2\Omega\eta},\quad R_o\equiv\frac{\eta}{r_{\mathrm{cmb}}^2},\quad E\equiv\frac{\nu}{r_{\mathrm{cmb}}^2},\quad q_\kappa\equiv\frac{\kappa}{\eta}, \tag{4}$$

where α_T is the core fluid thermal expansion, g_0 is the gravitational acceleration at the CMB, h_T is the negative temperature gradient of the prevailing state Θ_0 at the ICB, and κ is the thermal conductivity of the core fluid.

[16] Both the velocity field $\boldsymbol{v}$ and the magnetic field $\boldsymbol{B}$ are solenoidal, and thus described by the following poloidal and toroidal decomposition:

$$\boldsymbol{v}=\boldsymbol{\nabla}\times(T_v\hat{\mathbf{r}})+\boldsymbol{\nabla}\times\boldsymbol{\nabla}\times(P_v\hat{\mathbf{r}}), \tag{5}$$

$$\boldsymbol{B}=\boldsymbol{\nabla}\times(T_b\hat{\mathbf{r}})+\boldsymbol{\nabla}\times\boldsymbol{\nabla}\times(P_b\hat{\mathbf{r}}), \tag{6}$$

where $\hat{\mathbf{r}}$ is the unit radial vector. P and T in the equations are often called the poloidal and toroidal scalars, respectively. They are approximated by spherical harmonic expansions up to degree L and order M:

$$\begin{bmatrix}P_v\\T_v\\P_b\\T_b\end{bmatrix}=\sum_{m=0}^{M}\sum_{l=m}^{L}\begin{bmatrix}v_l^m(r)\\\omega_l^m(r)\\b_l^m(r)\\j_l^m(r)\end{bmatrix}Y_l^m(\theta,\phi)+\mathrm{CC}, \tag{7}$$

where (r, θ, ϕ) are the spherical coordinates, Y_l^m are the spherical harmonic functions of degree l and order m, and CC is the complex conjugate. The temperature perturbation Θ is expanded similarly.

[17] It should be noted that (1) and (5) imply that the Boussinesq approximation is used in the dynamo model, in which the fluid is assumed incompressible except for the buoyancy effect (the term with the Rayleigh number R_{th} in (1)).

[18] In the D″ layer, (2) is reduced to a simple diffusion equation

$$\frac{\partial\boldsymbol{B}}{\partial t}=\eta_{do}\nabla^2\boldsymbol{B}, \tag{8}$$

where $\eta_{do}\equiv\eta_d/\eta_o$. Above the D″ layer, the magnetic field $\boldsymbol{B}$ is a potential field, i.e.,

$$\boldsymbol{B}=-\boldsymbol{\nabla}\Phi,\quad\nabla^2\Phi=0. \tag{9}$$

The magnetic potential Φ can also be expanded in spherical harmonics and this will be discussed further in section 2.2. Finally, spatial discretization is carried out in the radial direction using a fourth-order finite difference approximation, with N_r grid points. All of the experiments presented in this paper use $N_r = L = M = 40$.

2.2. Geomagnetic Observations

[19] In field modeling, the magnetic potential Φ can be expanded as

$$\Phi=\sum_{0\le m\le l}^{l\le L_{\mathrm{obs}}}\psi_l^m(r)\,Y_l^m(\theta,\phi)+\mathrm{CC}, \tag{10}$$

where L_{obs} is the highest degree of the observable coefficients.

[20] Surface geomagnetic observation is carried out by measuring 3 components of the magnetic field $\boldsymbol{B}$ at ground stations, via airborne or spaceborne instruments. From these data, the spherical harmonic coefficients $\psi_{sl}^m\equiv\psi_l^m(r_{\mathrm{ea}})$ at the surface r_{ea} of the Earth are derived from various field models [e.g., *Sabaka et al.*, 2002]. Because of the crustal magnetization, $L_{\mathrm{obs}}\le 14$.

[21] By (9), one can find that

$$\psi_l^m\propto\frac{1}{r^{l+1}} \tag{11}$$

to ensure Φ remains bounded at infinity. This can then be used to obtain ψ_l^m at the top of the D″ layer from those ψ_{sl}^m at the Earth's surface. From (6), (7), (9) and (10), one can obtain that

$$b_l^m=\frac{r}{l}\psi_l^m\qquad\text{for}\qquad r\ge r_{\mathrm{dp}}. \tag{12}$$

Together with (11), we have

$$b_l^m(r_{\mathrm{dp}})=\frac{r_{\mathrm{dp}}}{l}\left(\frac{r_{\mathrm{ea}}}{r_{\mathrm{dp}}}\right)^{l+1}\psi_{sl}^m. \tag{13}$$

Equation (13) is generally referred to as the surface observation being downward continued to the top of the D″ layer, which can then used for assimilation.

2.3. Assimilation Algorithm

[22] While geomagnetic data assimilation is a new area of research, atmospheric and oceanic data assimilation have longer histories, including an established notation to represent the different variable types, operators and errors. In spite of the difference in application presented here we can still follow this notation, as described by *Ide et al.* [1997], fairly closely. A few changes have been made to avoid conflicts with geomagnetic variables.

[23] We can represent the numerical model of equations (1)–(3) as

$$\mathbf{x}^f(t_{k+1}) = \mathbf{M}\left[\mathbf{x}^f(t_k)\right], \tag{14}$$

where $\mathbf{x}^f(t_k)$ represents the forecast of the state (which includes velocity, magnetic field and temperature perturbation) at time t_k, and $\mathbf{M}()$ is the nonlinear numerical model (or MoSST core dynamics). The state vector is therefore of length $5LMN_r$, and for the computations in this paper, we take $L = M = N_r = 40$.

[24] The true state is updated by

$$\mathbf{x}^t_{k+1} = \mathbf{M}[\mathbf{x}^t(t_k)] + \boldsymbol{\epsilon}^m(t_k), \tag{15}$$

where $\mathbf{x}^t(t_k)$ is the true state at time t_k and $\boldsymbol{\epsilon}^m(t_k)$ represents the model error, which is assumed to be a zero mean noise process. The unbiased model assumption very often does not hold, as in the present work. We discuss the implications of this in section 5.

[25] The forecast calculation (14) is carried out until observations are made at times $(t_a)_j = (t_a)_{j-1} + \delta t_a$, where δt_a is the time between analyses. The observing process is given by

$$\mathbf{y}^o_k = \mathbf{H}_k[\mathbf{x}^t(t_k)] + \boldsymbol{\epsilon}^o_k, \tag{16}$$

where $\mathbf{H}_k$ is called the observation operator and $\boldsymbol{\epsilon}^o$ is the observation error, which is also generally assumed to be zero mean noise process. $\boldsymbol{\epsilon}^o$ includes errors due to crust and mantle losses, measurement errors, and field modeling errors (when the spectral coefficients from field models are used as observations). In general, $\mathbf{H}_k$ may be nonlinear and time-dependent, but for the present work it is linear and time-independent, and we write it as

$$\mathbf{y}^o_k = \mathbf{H}\mathbf{x}^t(t_k) + \boldsymbol{\epsilon}^o_k. \tag{17}$$

It is convenient to carry out the assimilation in spectral space because, as discussed in section 2.1, geomagnetic field models provide spherical harmonic coefficients ψ^m_{sl} of the geomagnetic potential Φ at the surface of the Earth. In the MoSST core dynamics model, the magnetic field $\boldsymbol{B}$, and all other variables are described by the same expansion (7).

[26] Because real geomagnetic observations, $\mathbf{y}^o$, are restricted up to degree $L_{\text{obs}} \leq 8$, the $\mathbf{H}$ operator zeros out the other variables and higher degree terms. In addition, via (13), $\mathbf{H}$ transforms the poloidal scalar coefficients b^m_l at the top of the D'' layer into surface geopotential coefficients ψ^m_{sl}.

[27] We use an optimal interpolation (OI) sequential assimilation framework [*Lorenc*, 1986] for this system. The analysis step, carried out every δt_a time units, is

$$\mathbf{x}^a(t_k) = \mathbf{x}^f(t_k) + \mathbf{K}_k\left[\mathbf{y}^o_k - \mathbf{H}\mathbf{x}^f(t_k)\right], \tag{18}$$

where $\mathbf{K}$ is the gain matrix, which is given by

$$\mathbf{K}_k = \mathbf{P}^f_k\mathbf{H}^T\left[\mathbf{H}\mathbf{P}^f_k\mathbf{H}^T + \mathbf{R}_k\right]^{-1}. \tag{19}$$

In equation (19), $\mathbf{P}^f_k$ and $\mathbf{R}_k$ are the forecast error covariance and the observation error covariance matrices, respectively. Thus the gain matrix $\mathbf{K}_k$ is chosen so as to minimize the analysis error variance (minimum variance estimate) and it weights the forecast and the observations relative to their respective error statistics.

[28] Very little is known about forecast error characteristics for geodynamo models, so it is most sensible to keep the estimate of $\mathbf{P}^f_k$ relatively simple. For example, cross covariances between different state variables are not yet well understood, and there are not any accurate estimates of correlation length scales. Ideally, the forecast error covariance would evolve in time according to the model dynamics [see, e.g., *Cohn*, 1997], but the high computational cost coupled with limited knowledge of model error make this unworkable. For the present study we therefore assume that the covariance is univariate (no cross variable correlations) and that there is no coupling between spectral modes. The error variance is assumed to be a constant function of radius (so we can drop the subscript k here and for the gain matrix $\mathbf{K}$ as well), and the error correlations decay linearly with length scale r_c. Thus the i, j^{th} entry in $\mathbf{P}^f$ can be written as

$$P^f_{i,j} = \sigma_i\sigma_j\rho_{i,j} = \sigma^2\rho_{i,j}, \tag{20}$$

where σ^2 is the forecast error variance, and the forecast error correlation, $\rho_{i,j}$ is

$$\rho_{i,j} = 1 - \frac{|r_i - r_j|}{r_c} \quad |r_i - r_j| < r_c \tag{21}$$

$$= 0 \qquad |r_i - r_j| \geq r_c. \tag{22}$$

[29] We assume that the observation errors are much smaller than the forecast errors, so that $\mathbf{R}_k$ can be dropped from equation (19). We will show in section 4 that this is a reasonable assumption for this particular set of OSSEs. We define the observation operator separately for each spherical harmonic wave number, $\mathbf{H}_l$, and it is restricted to just the poloidal magnetic field (since it all the other variables are unobserved),

$$\mathbf{H}_l = \begin{cases} \dfrac{lr^l_{dp}}{r^{l+1}_{\text{ea}}} & [\ 0\ \ 0\ \ ..\ \ 0\ \ 0\ \ 1\ ] \quad l \leq 8 \\ & [\ 0\ \ 0\ \ ..\ \ 0\ \ 0\ \ 0\ ] \quad l > 8 \end{cases} \tag{23}$$

Table 1. The 12 OSSEs Carried Out in This Study[a]

	No Model Error (a)		With Model Error (b)	
	$\mathbf{x}_I$	$\mathbf{x}_{II}$	$\mathbf{x}_I$	$\mathbf{x}_{II}$
A, L_{obs} = 33, r_c = 120 km	AIa	AIIa	AIb	AIIb
B, L_{obs} = 8, r_c = 120 km	BIa	BIIa	BIb	BIIb
C, L_{obs} = 8, r_c = 320 km	CIa	CIIa	CIb	CIIb

[a]Assimilation start times are $\mathbf{x}_I$ and $\mathbf{x}_{II}$. With indices for the number of observations and correlation length (A, B, C); the assimilation starting time (1, 2) and whether the forecast includes just initial error or initial and model error (a, b).

The quantity

$$\frac{l r_{dp}^{l}}{r_{\mathrm{ea}}^{l+1}}$$

results from the downward continuation of the surface magnetic observation (equation (13)). Thus for each wave number, $\mathbf{H}_l$ is simply a row vector with only the last entry (corresponding to the grid point at the CMB) nonzero. In the same way, the gain matrix $\mathbf{K}_l$ is also defined separately for

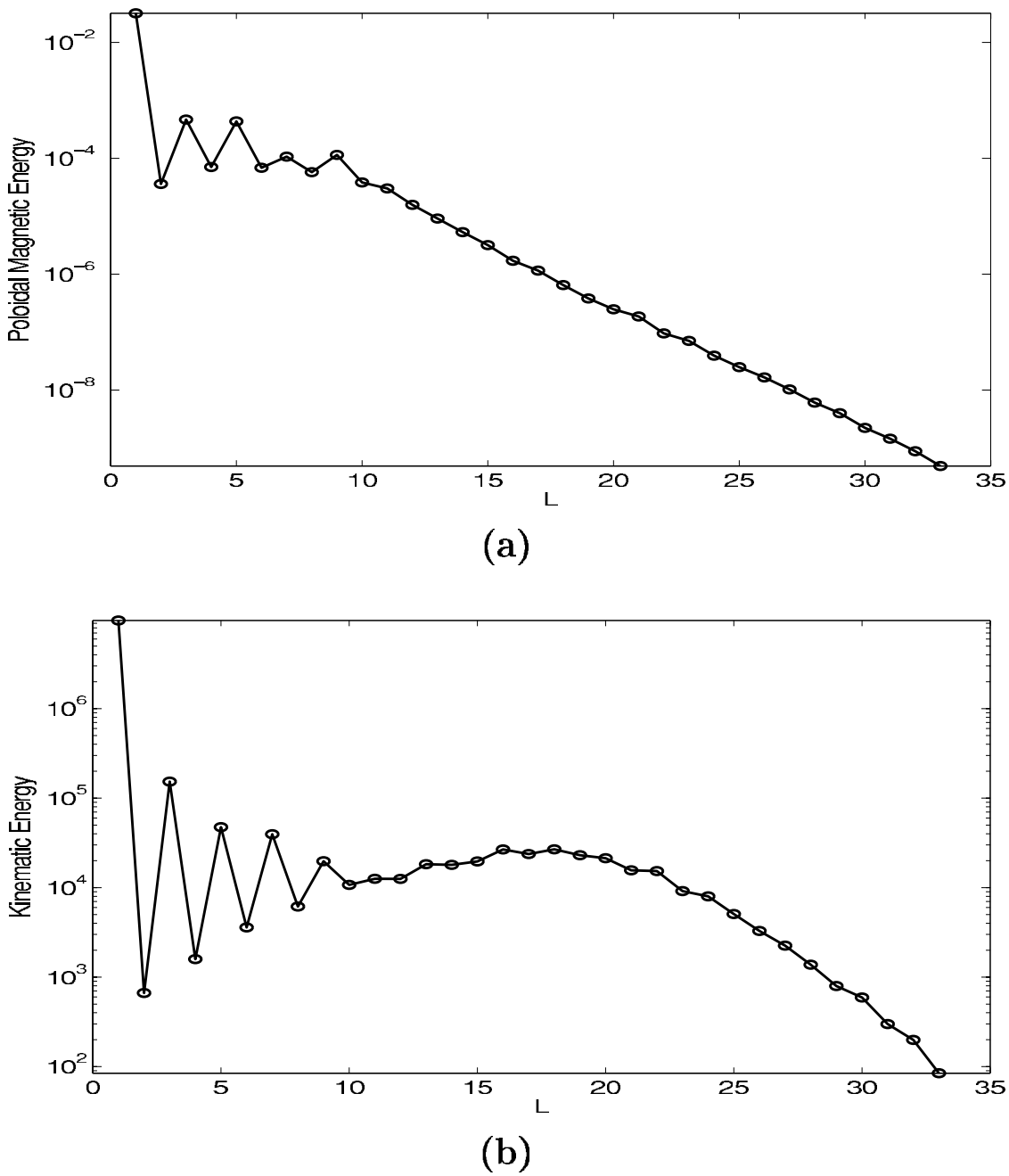

Figure 2. Time-averaged power spectra for the true solution as a function of l (summed over all m) for (a) poloidal magnetic field at the CMB and (b) the velocity magnitude at the CMB.

each wave number, so that for a given l, equation (19) becomes

$$\mathbf{K}_l = \left\{ \rho_{j,n} \frac{l r_{dp}^l}{r_{\mathrm{ea}}^{l+1}} \right\}, \tag{24}$$

where j is the radial component grid index, and $j = n$ is the grid point corresponding to the core mantle boundary. The gain in equation (18) therefore varies from $l r_{dp}^l / r_{ea}^{l+1}$ ($\rho_{j,n} = 1$) at r_{dp} to 0 ($\rho_{j,n} = 0$) at $r_{dp} - r_c$.

3. Observing System Simulation Experiments

[30] As shown by (13), surface geomagnetic observations can only provide spherical harmonic coefficients b_l^m (up to degree L_{obs}) for the poloidal scalar P_b of the magnetic field at r_{dp} the top of the D″ layer. Other state variables in the core, such as the velocity field $\boldsymbol{v}$, the temperature perturbation Θ and the toroidal scalar T_b of the magnetic field are not observable at all. Furthermore, the available record length for b_l^m is approximately 7000 years [*Korte and Constable*, 2005], much shorter than the history of the Earth, and is only a fraction of the magnetic free decay time τ_d ($\tau_d \approx 20{,}000$ years for the Earth's core). In addition, the parameters appearing in (1) and (3) are either not well known (the Rayleigh number R_{th}), or the values of the parameters used in numerical model are much larger than those appropriate to the Earth's core (the Rossby number R_o and the Ekman number E). Therefore one would not be surprised if the numerical dynamo solutions are not close to the dynamical processes in the outer core (the truth).

[31] To overcome these obstacles for geomagnetic data assimilation, we need to have some basic understanding of important issues such as the impact on the state vector in the outer core by the observation qualities (e.g., the degree L_{obs} and the time record length), the impact of parameter differences (model errors) on the model forecast and the impact of the initial state on data assimilation (initial errors). We use OSSEs to provide quantitative assessments of these issues.

[32] To understand the impact of the parameter values, we focus first on the Rayleigh number R_{th} in the OSSEs: Two different Rayleigh numbers are used in our analysis

$$R_{\mathrm{th}}^{(1)} = 15000 \quad \text{and} \quad R_{\mathrm{th}}^{(2)} = 14500, \tag{25}$$

while other parameters remain unchanged:

$$R_o = E = 1.25 \times 10^{-6}, \qquad q_\kappa = 1.0. \tag{26}$$

The difference in Rayleigh numbers can be also explained as the error between two models. The results can therefore be used to examine the impact of model errors on the assimilation.

[33] In the OSSEs, the sequential assimilations start from $t = t_a^{(0)}$ with the time interval δt_a between the two consecutive analyses. To understand the information incorporated into the state vector with respect to the assimilation history, we consider two sequences:

$$\begin{aligned} &\text{Case I} \qquad t_a^{(0)} = 0.10\tau_d; \\ &\text{Case II} \qquad t_a^{(0)} = 0.90\tau_d. \end{aligned} \tag{27}$$

In both cases, $\delta t_a = 0.01\tau_d$. Unless otherwise stated, in the rest of the paper, results of case I will be noted by the subscript "I", and those of case II will be noted by the subscript "II." To further simplify the discussion in the rest of the paper, we use the time scaled by the magnetic free-decay time τ_d. In this convention, $\delta t_a = 0.01$. The time step δt in numerical simulation is much smaller. Though it varies due the Courant-Friedrichs-Lewy (CFL) condition, but for most of the simulation, $\delta t \leq 10^{-4}\tau_d$.

[34] To understand how much information from observations is incorporated into the state vector of the system by the assimilation, one can compare unobserved variables of the forecast and of the true state.

[35] It is also useful to determine whether the initial state that is created by sequentially assimilating observations over a very long time period (e.g., a significant fraction of the magnetic free decay time) is more accurate than one created from a much shorter sequence of assimilations. If an initial state is closer to the true state in a dynamically consistent manner (i.e., without introducing artificial oscillations into the solution), then forecasts produced by running the model from this initial state should be more accurate than those from other initial states.

[36] OSSEs have been carried out using a nature run (truth) with $R_{\mathrm{th}}^{(1)}$. The assimilation is run with $R_{\mathrm{th}}^{(2)}$; and with $R_{\mathrm{th}}^{(1)}$, but using an initial state different from that of the nature run.

[37] We use an initial solution that is spun up with $R_{\mathrm{th}}^{(2)}$ so that all of the assimilation runs starting at $t_a^{(0)} = 0.1$ will have the same initial error. We refer to this initial state as $\mathbf{x}_{\mathrm{I}}^i$. Starting with this initial state, we use model parameters that are either identical to the true simulation (no model error) or continue with $R_{\mathrm{th}}^{(2)}$ (nonzero model error). Assimilations that start at a later time ($t_a^{(0)} = 0.95$) use a continuation of the free running model at $R_{\mathrm{th}}^{(2)} = 14{,}500$ (referred to as $\mathbf{x}_{\mathrm{II}}^i$). We use observing systems which contain either the full set of spectral modes ($L_{\mathrm{obs}} = 33$) or are restricted to $L_{\mathrm{obs}} = 8$, which is comparable to current field models accuracy for temporal variations. The observations are obtained by add-

Figure 3. The coefficient b_1^0 versus time for the poloidal magnetic field at $r = r_{dp}$ for experiments (a) AIb and AIIb, (b) AIa and AIIa, (c) BIb and BIIb, (d) BIa and BIIa (e), CIb and CIIb, and (f) CIa and CIIa. The assimilations have either model and initial error (Figures 3a, 3c, 3e); or initial error only (Figures 3b, 3d, and 3f). In each plot the true (nature) solution is given by squares, and the free running model is given by a dotted line. The assimilation which starts at $t_a^{(0)} = 0.1$ ($\mathbf{x}_{\mathrm{I}}$) is indicated by a solid line with triangles, and the assimilation that starts at $t_a^{(0)} = 0.95$ ($\mathbf{x}_{\mathrm{II}}$) is indicated by a dashed line with circles.

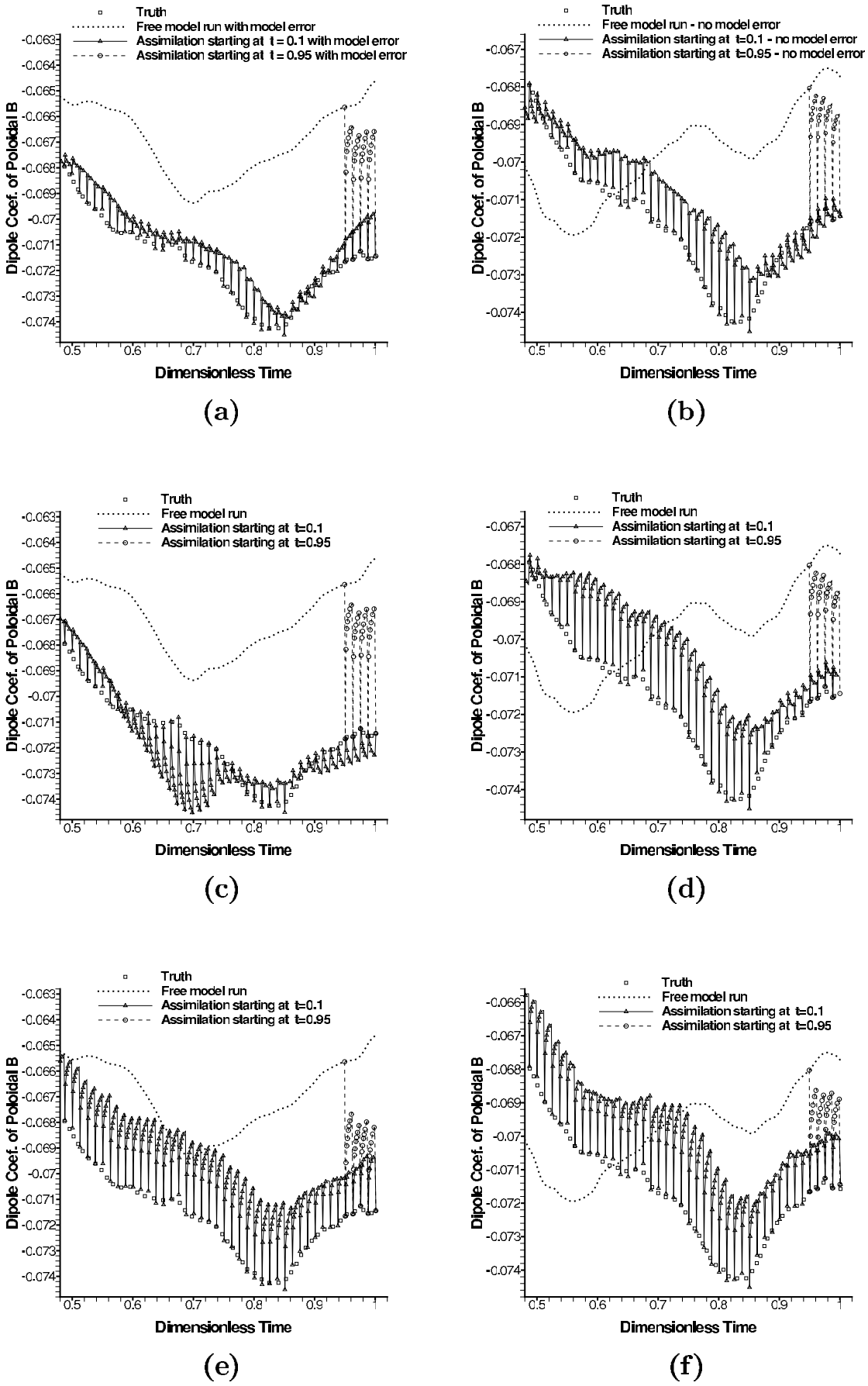
Truth
Free model run with model error
Assimilation starting at t = 0.1 with model error
Assimilation starting at t = 0.95 with model error
Dipole Coef. of Poloidal B
Dimensionless Time
(a)
Truth
Free model run - no model error
Assimilation starting at t=0.1 - no model error
Assimilation starting at t=0.95 - no model error
Dipole Coef. of Poloidal B
Dimensionless Time
(b)
Truth
Free model run
Assimilation starting at t=0.1
Assimilation starting at t=0.95
Dipole Coef. of Poloidal B
Dimensionless Time
(c)
Truth
Free model run
Assimilation starting at t=0.1
Assimilation starting at t=0.95
Dipole Coef. of Poloidal B
Dimensionless Time
(d)
Truth
Free model run
Assimilation starting at t=0.1
Assimilation starting at t=0.95
Dipole Coef. of Poloidal B
Dimensionless Time
(e)
Truth
Free model run
Assimilation starting at t=0.1
Assimilation starting at t=0.95
Dipole Coef. of Poloidal B
Dimensionless Time
(f)

Figure 3

ing Gaussian distributed noise with standard deviation σ^o = 1% of the poloidal field strength. Determining forecast error correlations generally involves a certain amount of physical reasoning and experimentation [*Stajner et al.*, 2001] to determine an optimal scale. Generally, flows with smaller-scale structures will have shorter error correlation lengths. If the length scale is allowed to become too long, observations will be correcting in locations where the local errors are in fact uncorrelated, and may also cause convergence problems. If they are too short, impact of the observations becomes too small. In these experiments we allow the forecast error correlation length take on values of r_c = 120 and r_c = 320 km in order to get an estimate of the optimal distance. A complete set of all possible combinations of the above parameter values would involve 24 separate assimilation runs, so we restrict our discussion to the following cases: experiment A, $L_{\rm obs}$ = 33, r_c = 120 km; experiment B, $L_{\rm obs}$ = 8, r_c = 120 km; and experiment C, $L_{\rm obs}$ = 8, r_c = 320 km. In each case the assimilation is carried out with and without model error, and are started from both $\mathbf{x}_{\rm I}^i$ and $\mathbf{x}_{\rm II}^i$. The 12 experiments are summarized in Table 1, which shows the labels for the experiments presented in Figures 2–9.

4. Results

[38] In this section we present the results to the assimilation experiments previously outlined. One goal of these experiments is to demonstrate how OSSEs can be used in geomagnetic data assimilation to quantify the relative success of an assimilation system. This approach also gives some indication as to how a given algorithm might be improved, by clearly showing whether unobserved fields (e.g., toroidal magnetic field) respond to changes in methodology, or whether the observable poloidal field can be drawn closer to the true state deep inside the core. The tests we propose here are comparison of time variation in spectral coefficients at the CMB, poloidal field RMS error near the CMB, forecast RMS errors for poloidal and toroidal fields as a function of radius, and predicted surface magnetic field morphology.

[39] Accurate observations of the entire spectrum could only be made in the absence of crustal field interference, and sufficiently sensitive instruments to overcome spatial modulation across the mantle. However, assimilation of full spectrum observations (L_{obs} = 33) is useful for since it gives an upper limit on the impact of surface observations for a given assimilation algorithm. Compared with assimilation of observations up to degree $L_{\rm obs}$ = 8, we can also learn how much the impact of observations on the analysis is reduced by this more realistic limitation.

[40] Forecast error correlations of r_c = 120 or 320 km imply that the impact of observations will reach the top 5.5% to 14.5% of the outer core. The optimal value for this distance is not currently known for geodynamo models, but carrying out assimilation helps us gain some insight on the range of possible values. If r_c is too short, observation impact will be limited to just the surface and the core state will be essentially unaffected. If r_c is set too long, corrections to the magnetic field will be too strong, possibly inducing nonphysical changes or even instabilities.

[41] Each experiment includes two sets of runs: one with model error (i.e., different Rayleigh numbers) and the other without.In both cases, the initial states for the experiments are set differently by carrying out numerical simulations with the two different Rayleigh numbers, each lasting for many magnetic free-decay times so that the solutions are well developed.

[42] In both sets (with and without model error), we continue the free model runs (without assimilation) for comparison with the assimilated solutions. These help us determine the extent of the impact of assimilating poloidal magnetic field observations on the estimate of the state of the core.

[43] Because the geodynamo flows are fairly complex and chaotic, it is useful to understand something of their power spectra. Figure 2a shows the poloidal magnetic power spectra and Figure 2b shows the total kinematic power spectra at the CMB. The exponential decay with wave number l indicates that the simulations are spatially resolved.

[44] Figure 3 shows the dipole component b_1^0 of the poloidal magnetic field as a function of time for each of the experiments. Experiment A ($L_{\rm obs}$ = 33 and r_c = 120 km) are shown in (a, b), experiment B ($L_{\rm obs}$ = 8 and r_c = 120 km) in (c, d) and experiment C ($L_{\rm obs}$ = 8 and r_c = 320 km) in (e, f). In each experiment Figures 3a, 3c, and 3e are the assimilation results with model and initial errors, and Figures 3b, 3d, and 3e are those with only the initial error. The true coefficients are represented by squares while the coefficients for the assimilation starting at $t_a^{(0)}$ = 0.1 ($t_a^{(0)}$ = 0.95) are given by triangles (circles) connected by a solid (dashed) line. The free model run is represented by a dotted line.

[45] In all experiments, the analysis times can be seen where the coefficients for the assimilation are drawn closer (but not exactly because of observation error) to the true values. After assimilation, values of the coefficients are shown for four different times of the forecast (triangles and circles). The plots are drawn starting around t = 0.5 so as to show the details of the assimilation cycles more clearly. The most significant feature of these coefficient trajectories is that rates of divergence (from the true state) are much greater for the $\mathbf{x}_{\rm II}$ forecasts than for the $\mathbf{x}_{\rm I}$ forecasts, in spite of the fact that the CMB coefficient values at the analysis times are exactly the same for the two cases. This implies that some improvement has been made to the estimate of the core state at each analysis time by carrying out a long assimilation run with observation information incorporated

Figure 4. Relative RMS error for the poloidal component of magnetic field in the D″ as a function of time. The assimilations are for experiments (a) A1b and AIIb, (b) AIa and AIIa, (c) BIb and BIIb, (d) BIa and BIIa, (e) CIb and CIIb, and (f) CIa and CIIa. Assimilations with both model and initial errors are shown in Figures 4a, 4c, and 4e and with the initial error only in Figures 4b, 4d, and 4f. The assimilations starting at $t_a^{(0)}$ = 0.1 ($\mathbf{x}_{\rm I}$) and $t_a^{(0)}$ = 0.95 ($\mathbf{x}_{\rm II}$) are indicated by triangles and squares, respectively. The error for the free running model is shown as a dotted line.

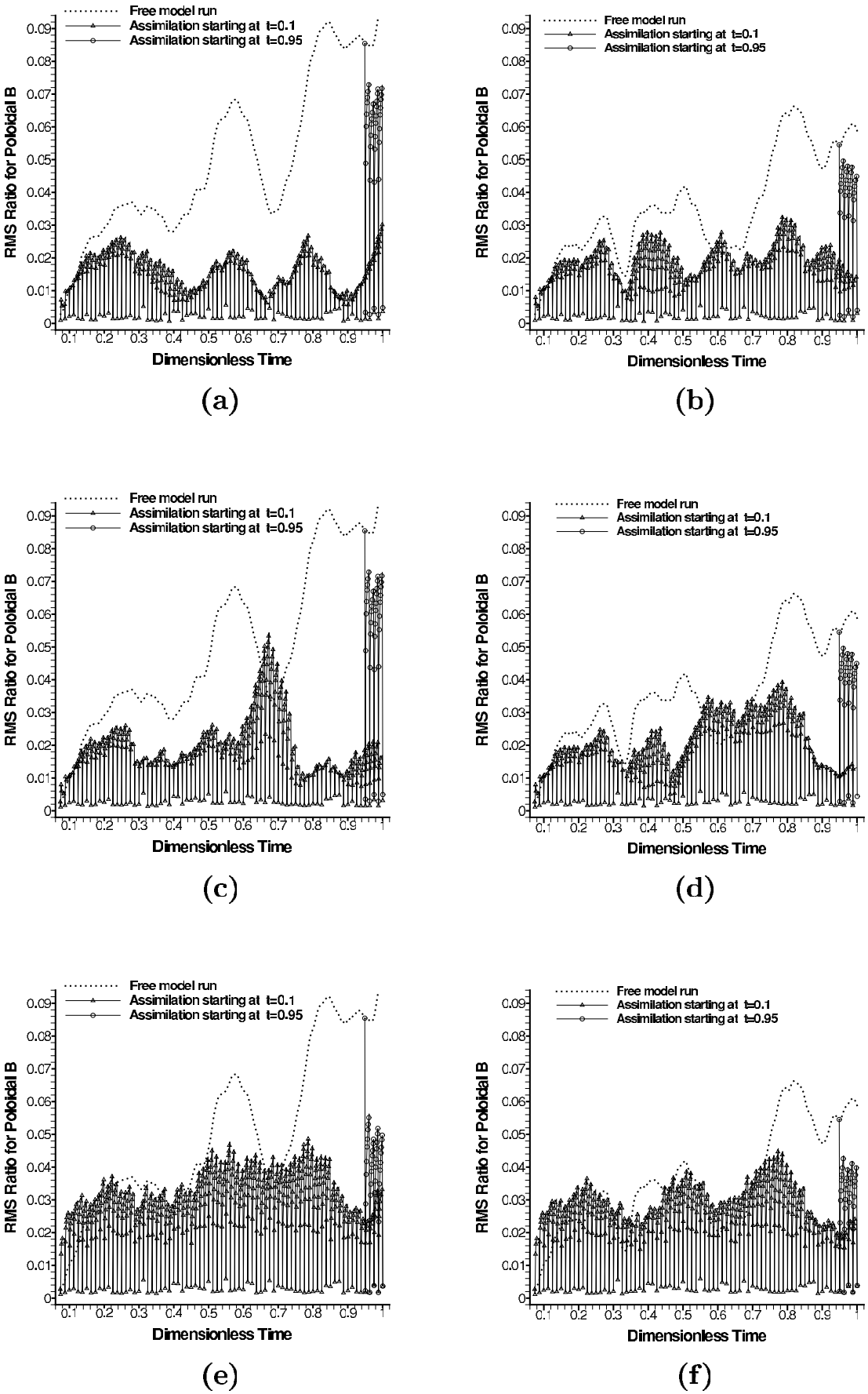
Free model run
Assimilation starting at t=0.1
Assimilation starting at t=0.95
RMS Ratio for Poloidal B
Dimensionless Time
(a)
(b)
(c)
(d)
(e)
(f)

Figure 4

over many assimilation cycles. For cases with model error, the first few analysis cycles show very little decrease in trajectory divergence, while this decrease is evident in the case without model error. Again this shows that in the absence of model error, the assimilation of observations is starting to draw the analysis state closer to the true state. This difference in error growth (or decay) between Figures 3a, 3c, and 3d and Figures 3b, 3d, and 3e is therefore an indicator of how parameter differences affect error growth.

[46] The effect of the degree of observations assimilated can be seen by comparing Figures 3b and 3d. During the first few analysis cycles, there appears to be very little difference in error growth between the $\mathbf{x}_{\mathrm{II}}$ forecasts in Figures 3b and 3d. However, the $\mathbf{x}_{\mathrm{I}}$ forecasts show some difference, with larger errors in the $L_{\mathrm{obs}} = 8$ case than in the $L_{\mathrm{obs}} = 33$ case. This indicates that over short time periods, the largest impact is from the low-degree (large-scale) components (which contain the most energy), but over longer time periods small-scale components begin to play observable role in decreasing errors. The impact of the forecast error correlation length can be seen by comparing (c) and (e). The $\mathbf{x}_{\mathrm{II}}$ forecasts are much closer to the truth with $r_c = 320$ km than with $r_c = 120$ km, indicating that larger r_c has a greater impact in the initial stages of the assimilation. However, the $\mathbf{x}_{\mathrm{I}}$ forecasts show that after a long period of time, the shorter r_c results in smaller errors. This implies that the forecast errors are correlated at length scales shorter than 320 km, though further cases are needed to come up with a more precise length.

[47] A more complete picture of the poloidal field error growth at the CMB can be obtained by calculating a relative RMS error summed over all of the coefficients:

$$\mathrm{RMS}_b(r) \equiv \left[\frac{\sum_{0\le m\le l}^{1\le l\le L}\left|b_l^{mf}(r) - b_l^{mt}(r)\right|^2}{\sum_{0\le m\le l}^{1\le l\le L}\left|b_l^{mt}(r)\right|^2}\right]^{1/2}. \tag{28}$$

Accumulation of RMS in the D″ layer

$$\mathrm{RMS}_{\mathrm{D}} = \int_1^{r_{\mathrm{dp}}} dr \mathrm{RMS}_b(r) \tag{29}$$

deserves special attention. In (29), the nondimensional $r = 1$ is the CMB.

[48] Figure 4 shows RMS_D for each of the cases described in Figure 3. These verify that the conclusions made from the dipole component trajectories can be extended to the entire set of coefficients for the poloidal field at the CMB. Again we see that compared to $L_{\mathrm{obs}} = 33$, restricting observation to $L_{\mathrm{obs}} = 8$ does not dramatically increase forecast errors, and that forecast error correlation length scales are likely closer to $r_c = 120$ km than to $r_c = 320$ km. Figure 4 also verifies that the assumption in section 2.2 that at analysis times, the forecast errors are much larger than the observation errors.

[49] Figure 5 shows the snapshots of $\mathrm{RMS}_b(r)$ in radius at a single time, $t = 0.988$. Here the immediate impact of the observations can be seen from the $\mathbf{x}_{\mathrm{II}}$ forecast (circles), which decrease to nearly zero at the CMB ($r = 1$) and remain distinctly smaller than the free model errors (dotted line) down to about $r = 0.9$ (which corresponds to the nondimensional forecast correlation length, r_c/r_{cmb}). As the assimilation proceeds in time, the improvement to the poloidal field runs deeper into the core. The $\mathbf{x}_{\mathrm{I}}$ forecast (triangles) shows a reduction in RMS_b to at least $r = 0.6$ in all cases. This is an indication that the assimilation of observations into the geodynamo model can make accumulative improvements to the state within the core, and far from the actual observation locations. The improvements run deeper in the absence of model error, and there is little apparent advantage to assimilating the full spectrum of observations.

[50] We next consider the RMS error of the completely unobserved toroidal field coefficients j_l^m,

$$\mathrm{RMS}_j(r) \equiv \left[\frac{\sum_{0\le m\le l}^{1\le l\le L}\left|j_l^{mf}(r) - j_l^{mt}(r)\right|^2}{\sum_{0\le m\le l}^{1\le l\le L}\left|j_l^{mt}(r)\right|^2}\right]^{1/2}, \tag{30}$$

shown in Figure 6. Here the reduction in RMS_j is also clear, particularly at longer assimilation times. There is a small reduction in the $\mathbf{x}_{\mathrm{II}}$ forecast (only when there is model error), and a larger reduction to about $r = 0.7$ in the $\mathbf{x}_{\mathrm{I}}$ forecast. There is no advantage to assimilating the full spectrum observations, and the shorter error correlation length, $r_c = 120$ km again results in a bigger drop in forecast error.

[51] The reductions in RMS errors of the poloidal field and toroidal field coefficients imply that after a long assimilation time, forecast of the poloidal and toroidal fields near the CMB improve significantly. This could lead to additional geophysical applications, e.g., core-mantle interactions where the toroidal field is critical for a finite Lorentz torque.

[52] Figures 7 and 8 show the surface poloidal field morphology at $t = 0.988$ and $t = 0.992$ from the true state (Figures 7a and 8a), the free running model with no model error (Figures 7b and 8b), the forecast $\mathbf{x}_{\mathrm{I}}$ (Figures 7c and 8c), and the forecast $\mathbf{x}_{\mathrm{II}}$ (Figures 7d and 8d) (both with no model error). Correlations between the forecast states and the true state, $\rho(\Delta\mathbf{r})$ at each time are plotted in (e) and (f), using

$$\rho(\Delta\mathbf{R}) = \frac{\overline{\left[B_f(\mathbf{r}+\Delta\mathbf{r}) - \overline{B_f(\mathbf{r}+\Delta\mathbf{r})}\right]\left[B_t(\mathbf{r}) - \overline{B_t(\mathbf{r})}\right]}}{\sqrt{\overline{\left[B_f(\mathbf{r}+\Delta\mathbf{r}) - \overline{B_f(\mathbf{r}+\Delta\mathbf{r})}\right]^2}}\sqrt{\overline{\left[B_t(\mathbf{r}) - \overline{B_t(\mathbf{r})}\right]^2}}}, \tag{31}$$

where the over bar indicates the mean of the variable.

Figure 5. $\mathrm{RMS}_b(r)$ at $t = 0.988$ for experiments (a) AIa and AIIa, (b) AIb and AIIb (c), BIa and BIIa, (d) BIb and BIIb, (e) CIa and CIIa, and (f) CIb and CIIb. Assimilations with both model and initial error are shown in Figures 5a, 5c, and 5e and with initial error only in Figures 5b, 5d, and 5f. The assimilations starting at $t_a^{(0)} = 0.1$ and $t_a^{(0)} = 0.95$ ($\mathbf{x}_{\mathrm{I}}$ and $\mathbf{x}_{\mathrm{II}}$) are indicated by triangles and squares, respectively. The free running model error is shown as a dotted line.

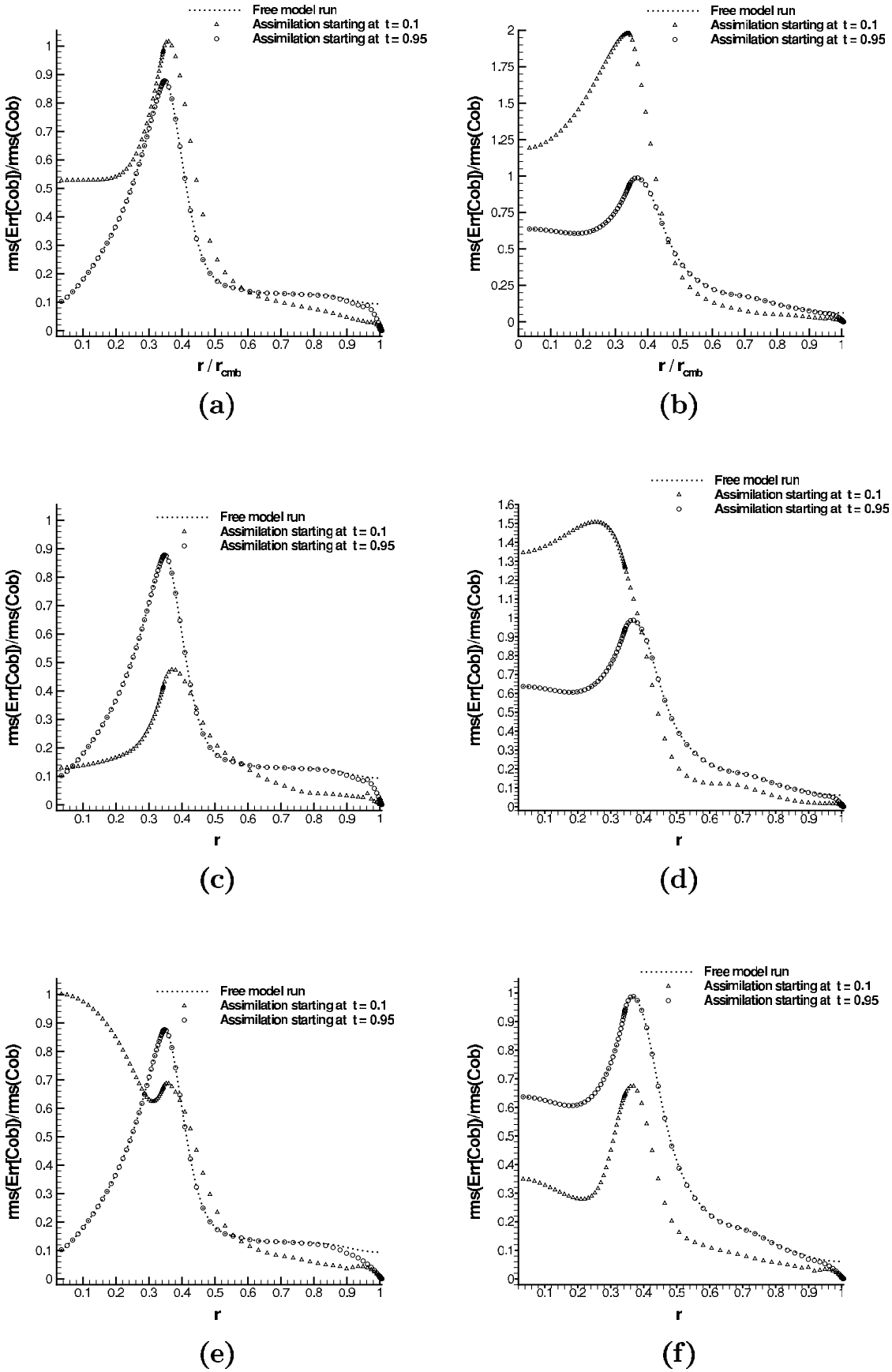
Free model run
Assimilation starting at t = 0.1
Assimilation starting at t = 0.95
rms(Err[Cob])/rms(Cob)
r / r_cmb
r
(a)
(b)
(c)
(d)
(e)
(f)

Figure 5

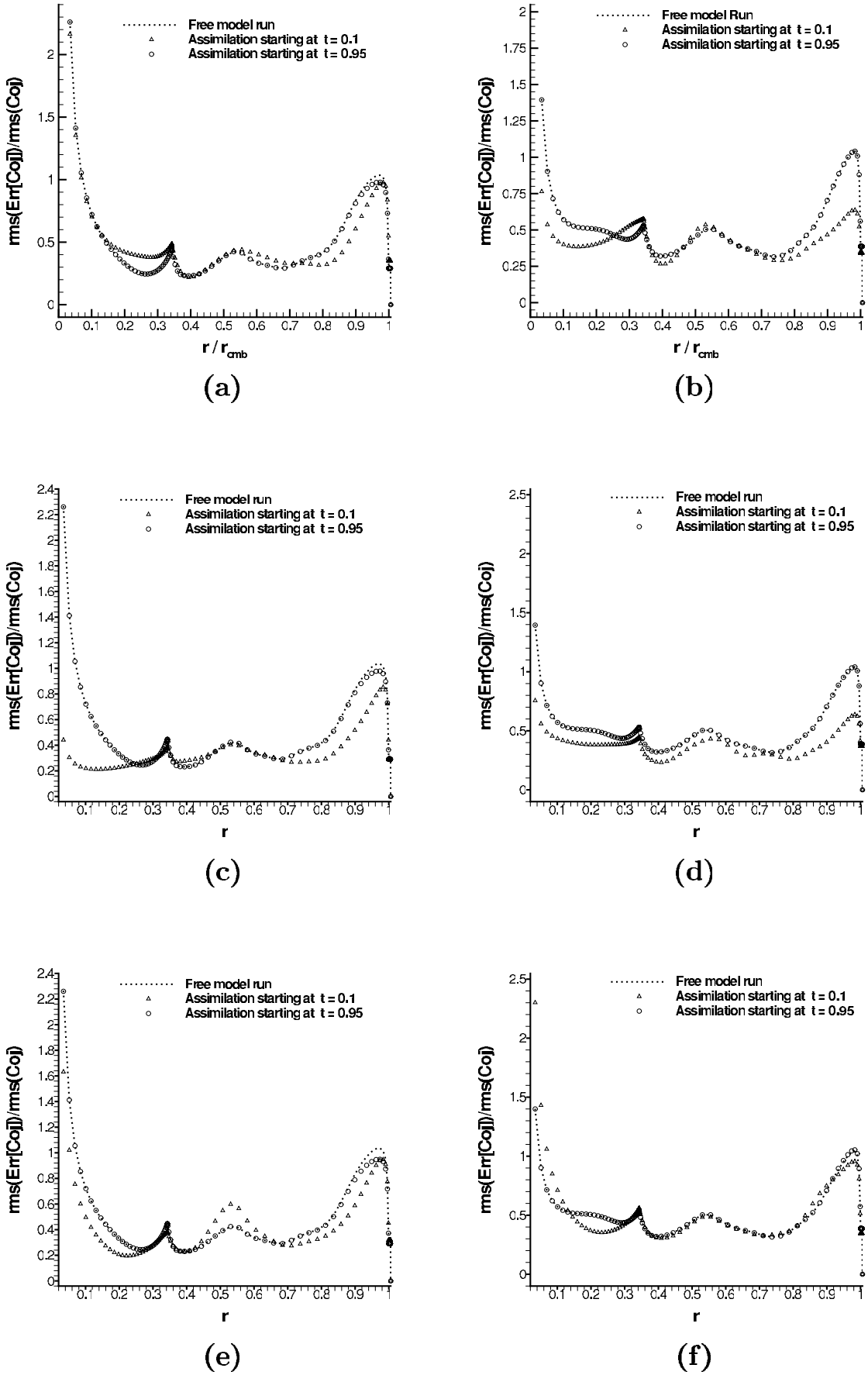

Figure 6. Similar to Figure 5, but for $RMS_j(r)$.

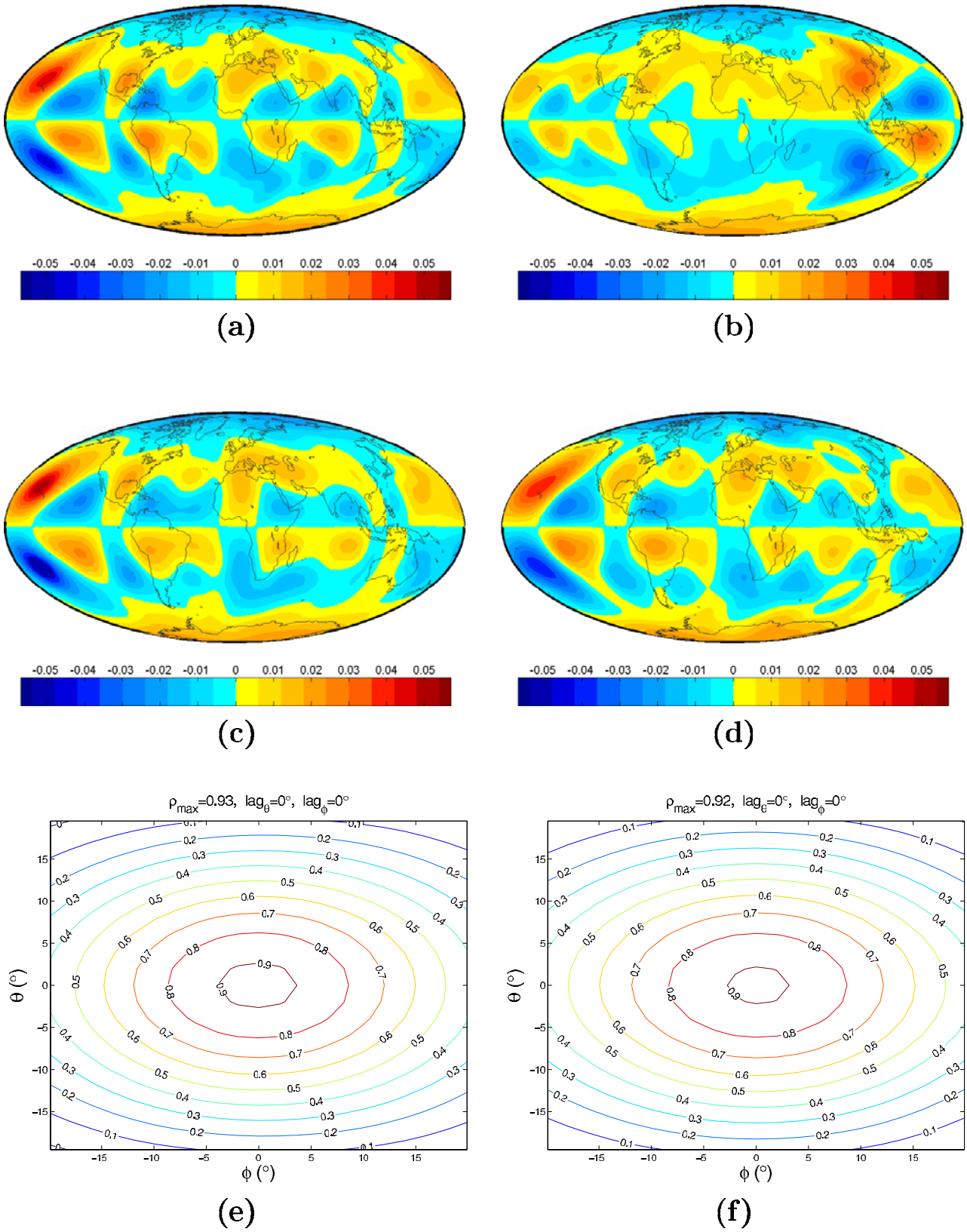

Figure 7. Surface morphology of B_r at $t = 0.988$, for (a) the true solution, (b) the free running model, (c) BIa, (d) BIIa correlation distribution $\rho(\Delta\mathbf{R})$ between the fields in Figures 7c and 7d and the true field (Figure 7a) are shown in Figures 7e and 7f, respectively. No model error is introduced in the free model run and forecast.

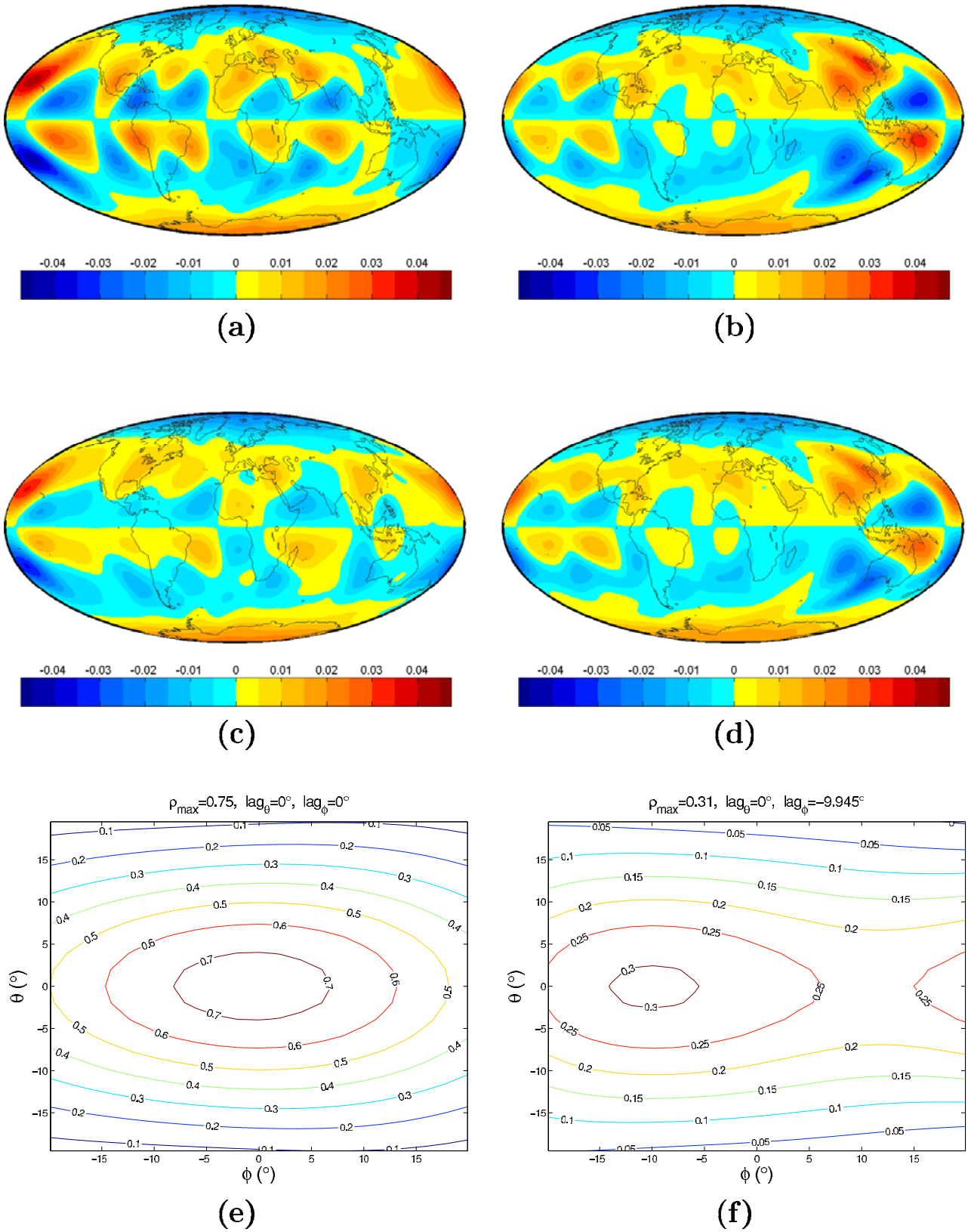

Figure 8. Similar to Figure 7, but at a later time $t = 0.992$.

[53] At $t = 0.988$, the free running model and the true field are very different (e.g., over North America and the Pacific). Both the $\mathbf{x}_{\mathrm{I}}$ and the $\mathbf{x}_{\mathrm{II}}$ are very close to the true field, with minor differences in intensity and no significant phase difference. At a later time $t = 0.992$, the two forecasts start to show increased errors, but the error growth rate is significantly larger for the $\mathbf{x}_{\mathrm{II}}$ forecast. Comparisons between Figures 7b and 8b and Figures 7d and 8d show that the latter is drawn toward the free running model as the forecast progresses which is particularly noticeable over southeast Asia and Australia. The correlation in Figures 7f and 8f shows that the maximum correlation has dropped to 0.3 and the zonal lag is now nearly 10°. In contrast, $\mathbf{x}_{\mathrm{I}}$ forecast retains much of the structure of the true state, but with significant decay in magnitude. The correlation in Figures 7e and 8e shows a maximum of 0.7 and no zonal lag. There is very little movement of the forecast field toward the free running model field.

[54] The impact of assimilating magnetic field observations on the velocity field is demonstrated in Figure 9, which shows the radial component on a spherical shell 35 3 km below the CMB at $t = 0.992$. Because the velocity field is only indirectly affected by the observations through the $\mathbf{J} \times \mathbf{B}$ term in equation (1). Therefore any improvement in the velocity field will occur gradually over a long time rather than suddenly at analysis times. Figure 9a shows the radial velocity field, while Figure 9b shows the free running model (without imposed model error). While both the true and free model states exhibit a similar equatorial wave number, the true state has a well defined phase shift between the equator and the poles, while the free model run is less well organized near the poles. Figures 9c and 9d show forecasts from the $\mathbf{x}_{\mathrm{I}}$ and $\mathbf{x}_{\mathrm{II}}$ assimilation runs respectively. The longer running assimilation (Figure 9c) has begun to organize very slightly with the same polar shift seen in the true state, while the shorter run (Figure 9d), is essentially identical to the free model run. The correlations between Figures 9c and 9d and the true state (Figure 9a), shown in Figures 9e and 9f, confirm that the $\mathbf{x}_{\mathrm{I}}$ run has a maximum correlation of 0.19, while for $\mathbf{x}_{\mathrm{II}}$ it is only 0.03.

5. Discussion

[55] In this paper we have described the framework for Observing System Simulation Experiments (OSSEs) developed with the purpose of demonstrating how it can be used to assess the success of a geomagnetic data assimilation system. To demonstrate its application, it has been used with an Optimal Interpolation (OI) assimilation system in which the parameters for the true and model states are close together. Through this demonstration, we have shown how OSSEs can be used to compare details of the state vector that are unavailable when using real physical observations. This allows us to compare variables deep inside the core to determine whether the impact of surface observations reaches them, and if so, when the impact is to draw the model closer to the true state of the system. This is important to understand whether and why the geomagnetic field forecast improves with one approach over another, and which variables or regions in the core are most sensitive to the surface magnetic field observations.

[56] Although application of OSSEs in this paper is mainly to demonstrate a systematic methodology for understanding and assessing the impact of surface observation on model solution variation (and thus forecast), the results shown in this paper represent the first detailed set of geomagnetic data assimilation OSSE experiments, and require further discussion.

[57] The OI algorithm employed here uses a univariate error forecast covariance which decays linearly with distance. This means that changes to the poloidal component beyond this correlation distance and to other state variables at all locations, can only happen through the model, and not through the analysis equations themselves. The experiments demonstrate this in Figure 5 because the forecast generated after just a few analysis cycles only shows corrections to the poloidal magnetic field to depths less than the correlation length, while the longer assimilation run shows improvements to the same field about halfway into the outer core. Experiments with a longer forecast error correlation length demonstrate that the assimilation is actually a little less accurate, which gives us some information on how errors are correlated within the geodynamo model. This also shows that the assimilation cannot be sped up by arbitrarily increasing this length scale. The toroidal component of magnetic field and the velocity field both show small but measurable improvements after a long a long assimilation run, as information from the poloidal magnetic field is passed through the model equations to the other variables. This implies that with a long enough assimilation, information can be obtained on the unobserved core flow variables.

[58] Speeding up the assimilation convergence, or more precisely, drawing the model solution closer to the true state more rapidly, is of great importance in geomagnetic data assimilation. Not only is the observation history short relative to the geodynamo time scales, but the earliest (and the longest) portion of the observation record is accurate to $L_{\mathrm{obs}} \leq 5$. However, this is where OSSEs can be extremely valuable in creating and testing algorithms that are optimal for the existing geomagnetic field models and geodynamo models. An artificial observation record could be created in which the degree of accuracy follows that of the physical record, thereby creating a realistic means to assess whether significant improvements can be made to both the core state estimates and magnetic field forecasts. This will allow us to focus on and test algorithms that can make corrections to all of the state variables through a multivariate error covariance. For example, *Borovikov et al.* [2005] has developed an ocean data assimilation system in which multivariate error covariances are calculated using a Monte Carlo approach. A system of this type can directly be tested using OSSEs to determine whether the assimilation has improved the accuracy of the model state, relative to a system using univariate error covariance.

[59] We must also address the issue of parameter values. We have deliberately chosen to create a difference between the true and model states through a small change in the Rayleigh number. This has allowed us to focus on issue of extracting information from the experiments, rather than the parameter values themselves. In fact, some of the parameters for the Earth's core are not well known, while some others have values too small to be implemented in numerical geodynamo models. In other words, parameter values

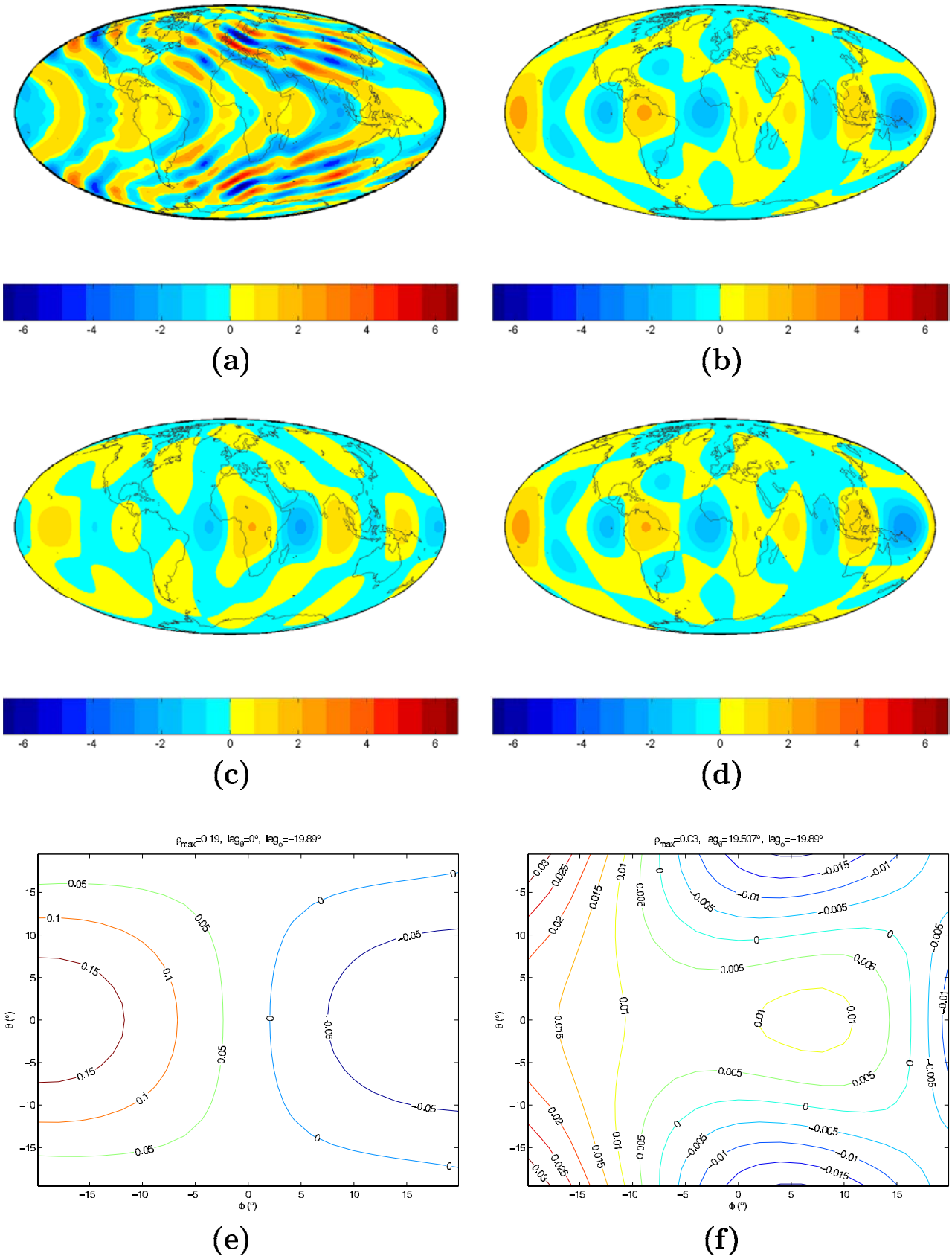

Figure 9. Radial Velocity V_r on a spherical shell 35 km below the CMB at t = 0.992, for (a) the true solution, (b) the free running model, (c) BIa, (d) BIIa correlation distribution $\rho(\Delta\mathbf{R})$ between the fields in Figures 9c and 9d and the true field (Figure 9a) are shown in Figures 9e and 9f, respectively. No model error is introduced in the free model run and forecast. All units are nondimensional.

used in numerical models are very different from those appropriate for the Earth's core. In addition, uncertainties exist in other physical properties, such as the boundary conditions (e.g., heterogeneity in the D″ layer or in the lower mantle).

[60] The valid question arises: how then can OSSEs tell us anything about how well a geomagnetic data assimilation system can handle real data? Larger computing platforms are becoming more generally available, allowing for increasingly wider variations in parameter spaces that can be computed with relative ease. Even though the geodynamo will remain intractable for some time, an increasing numerical parameter domain can tell more about how close we are from the real Earth. For example, an approximation to this problem can be made by creating a nature run with very high resolution (and accordingly stiffer parameter values), while the model used in the assimilation is designed to run with substantially lower resolutions. Thus the nature run parameters can be made beyond the capability of the assimilation run, thereby adding this fundamental issue of geomagnetic assimilation into the experiments.

[61] Finally, we return to the question of the impact of model biases on the assimilation, and how they might be overcome. Because most assimilation algorithms make the assumption of unbiased Gaussian distributed forecast errors, model bias will result in a less than optimal analysis. This means that the analysis errors will be larger than predicted by estimation theory. Recent work by *Dee and Da Silva* [1998] describes a bias correction scheme that removes the forecast bias in observed variables before assimilating observations. In geomagnetic data assimilation this would mean estimating and removing bias in the poloidal component of the magnetic field. This is an area of future work.

[62] **Acknowledgments.** The author's wish to thank A. Fournier for his careful review of the manuscript, which substantially improved the quality of the paper. This research is supported by the NSF Mathematical Geophysics program under the grant EAR-0327875, by NASA Solid Earth and Natural Hazard Program (SENH), and by NASA Mars Fundamental Research Program (MFRP).

References

Atlas, R. (1997), Atmospheric observations and experiments to assess their usefulness in data assimilation, *J. Meteorol. Soc. Jpn.*, *75*, 111–130.

Borovikov, A., M. M. Rienecker, C. L. Keppene, and C. C. Johnson (2005), Multivariate error covariance estimates by Monte-Carlo simulation for assimilation studies in the Pacific Ocean, *Mon. Weather Rev.*, *133*, 2310–2334.

Cohn, S. E. (1997), An introduction to estimation theory, *J. Meteorol. Soc. Jpn.*, *75*, 257–288.

Dee, D., and A. M. Da Silva (1998), Data assimimilation in the presence of forecast bias, *Q. J. R. Meteorol. Soc.*, *124*, 269–295.

Dormy, E., J. Valet, and V. Courtillot (2000), Numerical models of the geodynamo and observational constraints, *Geochem. Geophys. Geosyst.*, *1*(10), doi:10.1029/2000GC000062.

Evensen, G. (1994), Sequential data assimilation with a nonlinear quasi-geostrophic model using Monte Carlo method to forecast error statistics, *J. Geophys. Res.*, *99*, 10,143–10,162.

Fournier, A., C. Eymin, and T. Alboussiére (2007), A case for variational geomagnetic data assimilation: Insights from a one-dimensional, nonlinear, and sparsely observed MHD system, *Nonlinear Processes Geophys.*, *14*(3), 163–180.

Glatzmaier, G. A., and P. H. Roberts (1995), A three-dimensional self-consistent computer simulation of a geomagnetic field reversal, *Nature*, *377*, 203–209.

Houtekamer, P. L., and H. L. Mitchell (1998), Data assimilation using an ensemble Kalman filter technique, *Mon. Weather Rev.*, *126*, 697–811.

Ide, K., P. Courtier, M. Ghil, and A. C. Lorenc (1997), Unified notation for data assimilation: Operational, sequential and variational, *J. Meteorol. Soc. Jpn.*, *75*, 181–189.

Kageyama, A., and T. Sato (1997), Generation mechanism of a dipole field by a magnetohydrodynamical dynamo, *Phys. Rev. E*, *55*, 4617–4626.

Korte, M., and C. G. Constable (2005), The geomagnetic dipole moment over the last 7000 years—New results from a global model, *Earth Planet. Sci. Lett.*, *236*, 348–358.

Kuang, W., and J. Bloxham (1997), An Earth-like numerical dynamo model, *Nature*, *389*, 371–374.

Kuang, W., and J. Bloxham (1999), Numerical modeling of magnetohydrodynamic convection in a rapidly rotating spherical shell: Weak and strong field dynamo action, *J. Comput. Phys.*, *153*, 51–81.

Kuang, W., and B. F. Chao (2003), Geodynamo modeling and core-mantle interaction, in *The Core-Mantle Boundary Region*, *Geodyn. Ser.*, vol. 31, edited by M. Gurnis et al., pp. 193–212, AGU, Washington, D. C.

Larmor, J. (1919), How could a rotating body such as the Sun become a magnet, report, pp. 159–160, Br. Assoc. Adv. Sci., London.

Lorenc, A. C. (1986), Analysis methods for numerical weather prediction, *Q. J. R. Meteorol. Soc.*, *112*, 1177–1194.

Macmillan, S., and J. M. Quinn (2000), The 2000 revision of the joint UK/US geomagnetic field models and an IGRF 2000 candidate model, *Earth Planets Space*, *52*, 1149–1162.

Sabaka, T. J., N. Olson, and R. A. Langel (2002), A comprehensive model of the quiet-time near-Earth magnetic field: Phase 3, *Geophys. J. Int.*, *151*, 32–68.

Shankland, T. J., R. J. O'Connell, and H. S. Waff (1981), Geophysical constraints on partial melt in the upper mantle, *Rev. Geophys.*, *19*, 394–406.

Stajner, I., L. P. Riishojgaard, and R. B. Rood (2001), The geos ozone data assimilation system: Specification of error statistics, *Q. J. R. Meteorol. Soc.*, *127*, 1069–1094.

Sun, Z., A. Tangborn, and W. Kuang (2007), Data assimilation in a sparsely observed one-dimensional modeled mhd system, *Nonlinear Processes Geophys.*, *14*(3), 181–192.

Talagrand, O. (1997), Assimilation of observations, an introduction, *J. Meteorol. Soc. Jpn.*, *75*, 191–209.

W. Kuang, Planetary Geodynamics Laboratory, Code 698, NASA Goddard Space Flight Center, Greenbelt, MD 20771, USA. (weijia.kuang-1@nasa.gov)

D. Liu and A. Tangborn, Joint Center for Earth Systems Technology, University of Maryland, Baltimore County, Baltimore, MD 21250, USA. (donliu@umbc.edu; tangborn@umbc.edu)